Volumetric Flow Characterisation of a Rectangular Orifice Impinging Synthetic Jet with Single-camera Light-field PIV

Zhou Zhao[1], Junfei Ding[1], Shengxian Shi[1*]
Rene Kaufmann[2], Bharathram Ganapathisubramani[2*]

[1] Shanghai Jiao Tong University, School of Mechanical Engineering, Shanghai, China

[2] University of Southampton, Faculty of Engineering and the Environment, Southampton, UK

*kirinshi@sjtu.edu.cn

*G.Bharath@soton.ac.uk

Abstract

The formation and evolution of volumetric flow structures from a rectangular orifice synthetic jet ($AR = 10$, $Re = 550$, $Sr = 0.0117$, and $L_o = 0.0855m$) impinging on a flat plate is investigated using phase-locked single-camera light-field particle image velocimetry (LF-PIV). An impinging plate is located 24 orifice widths away from the rectangle orifice and this volumetric flow data is used to capture the mechanisms involved in the interaction. Flow statistics and structure information obtained by time-averaging and phase-averaging the volumetric data reveal the formation and evolution of three-dimensional vortical structures and sweeping vortex that characterise the flow-surface interaction.

Keywords: Rectangular Synthetic jet, Jet impingement, Light-field PIV

1 Introduction

Synthetic jet, also known as zero-net-mass-flux (ZNMF) jet, is normally generated by an oscillating membrane or piston in cavity which pushes fluids through an orifice into external quiescent fluid (ejection phase) then sucks the same mass fluids back into the cavity (suction phase), with no net mass flow through the orifice [1]. At ejection phase, the issued fluid separates at sharp edges of orifice and forms a roll-up structure with a vortex ring, which is found too far downstream from the orifice to be drawn into the cavity and keeps propagating downstream under its self-induced velocity. This creates a ZNMF flow with non-zero streamwise momentum. Synthetic jet has attracted considerable amount of attentions in the last two decades, and has been widely studied both numerically [2–6] and experimentally [7–9]. Compact hardware as well as low energy

consumption have found synthetic jet in many applications, such as flow control [10–14], virtual aero-shaping [15], thrust vectoring [16,17], heat transfer [18–21] and propulsion [22,23].

Based on its orifice geometry, synthetic jet can be divided into axisymmetric (e.g. circular) and non-axisymmetric (e.g. rectangular) ones. Researches have focused on circular jets and provided detailed insights into the influence of key parameters on flow structures [4,6,9,24]. In addition, studies on rectangular (or slot, finite-span) synthetic jet started with high aspect-ratio (AR) slot orifices [7,25], which was found that these flows can be treated as two-dimensional (2D) jet flow. Later on, Amitay and Cannelle [26] applied two-dimensional particle image velocimetry (2D-PIV) to study the effect of AR on the development of synthetic jet and the spatial evolution of secondary three-dimensional (3D) vortical structures. It was suggested that 3D experimental studies are necessary to correctly capture the three-dimensionalities associated with the secondary spanwise structures. To make further study, Buren et al. [27,28] investigated the effect of AR and Reynolds number (Re) on the flow structures of a finite-span synthetic jet by stereoscopic particle image velocimetry (SPIV). It was found that the velocity and vorticity fields are greatly affected by Re, with the lowest Re case producing the highest normalised peak velocities and vorticity. Also, the evolution of vortex ring in different AR and Re was presented. It was concluded that the axis-switching location increased with Re and AR. The experimental results also indicated that an increasing AR can lead to a stronger presence of secondary structures but a decreased size of the structures, when comparing synthetic jets of AR $= 6,12,18$. Thus, a synthetic jet with relatively low AR can present enough detectable characterised details. However, the measurements had to be conducted for several planes along both major-axis and minor-axis, so as to reconstruct a 3D volume by combining all measurement planes. Within this volume, vortex ring evolution was analysed by the constructed ring lines, which could present some basic characteristics of the vortex ring. Thus, more detailed 3D vortical structures remained to be investigated. Recently, Wang et al. [29–31] utilised dye visualisation, time-resolved 2D-PIV, and time-resolved SPIV to investigate vortical structures for rectangular synthetic jet. They identified two kinds of streamwise vortices and one arc-like vortical structures, in addition to the main vortex ring. The evolution of 3D vortical structures was also presented in a more detailed and intuitive way.

With studies on free synthetic jets get into deeper, significant attention has been paid on synthetic jet impingement for its potential high efficiency in cooling applications [20,32]. Efforts were

initially focused on heat transfer mechanisms of round orifice synthetic jet impingement, to explore the influence of key parameters as Re, stroke length (L_o), orifice-to-plate distance, and actuator frequency [19,33]. To better examine flow characteristics of circular orifice synthetic jet impingement, McGuinn et al. [34] studied the effect of L_o on vortex ring evolution. It was found that four flow morphology regimes can be identified based on different threshold values of L_o. Further studies were made to experimentally investigated the influence of Strouhal number (Sr) and orifice-to-plate distances on the flow field [35]. It was concluded that flow features highly depend on Sr and orifice-to-plate distance as the former governs the presence and relative importance of vortex ring and trailing jet, whereas the latter delimits the downstream evolution of these structures. Recently, a more detailed experimental study on the effects of L_o and Re was performed via time-resolved 2D-PIV [36]. The vortex evolutions during impingement were described by phase-averaged vorticity fields and linked with wall-fields via instantaneous wall pressure and wall shear stress distributions. It was also found that the effect of L_o is mainly reflected in the vortex ring coherence before impacting the wall.

On the other hand, rectangular synthetic jet impingement has recently drawn considerable attention for its promising performance in heat transfer, and some preliminary researches have been made [18,37–40]. However, unlike the detailed studies on circular orifice synthetic jet impingement in both flow and heat transfer, only limited attentions were recently paid to the flow characterisation of the rectangular orifice synthetic jet impingement. A closely related study was performed by Fanning et al. [41], which mainly focused on a pair of adjacent synthetic jets. They provided detailed research via 2D-PIV on the effect of orifice-to-plate distance, orifice-to-orifice centre separation distance and phase difference, however, the discussions on the flow structures were mainly about the measurement results on the centre plane. Later, Ghaffari et al. [42] also investigated a slot synthetic jet impingement by 2D-PIV. The flow on the 2D slice along the centreline of the jet was visualised, while the three-dimensionalities of the structures were less discussed. Thus, it would be highly interesting to experimentally investigate the formation and evolution of 3D flow structures of a rectangle orifice synthetic jet, as well as how these structures would be affected when impinging onto a flat plate. To accomplish that, Tomographic PIV (Tomo-PIV) would be one of the “canonical” volumetric diagnostic tools for its high spatial resolution as well as measurement accuracy. However, its multi-camera system and the related volumetric calibration procedures may hamper the investigations being performed in a more concise and

efficient way. As an alternative, LF-PIV provides a new means for a convenient appreciation of volumetric flow field [43–45]. In a similar hardware setup as the traditional 2D-PIV, LF-PIV could provide snapshots of 3D velocity field for complex flows [46–48]. As such, the current study is made use of the phase-locked single-camera LF-PIV to study an AR = 10 rectangular impinging synthetic jet as a representative case. This effort could not only provide further investigation on this less-discussed topic, but also be an examination to see whether the single-camera LF-PIV is able to resolve such complex 3D flow field.

The paper is organised as follows: In Sect. 2, the experimental arrangement and governing parameters will be described. The phase-locked LF-PIV data processing will also be included, after which Sect. 3 will present the time-averaged and phase-averaged measurement results. The vortex evolution will also be discussed. Finally, a brief conclusion will be provided to summarise the main findings and performance of the LF-PIV in Sect. 4.

2 Experiment Details and Parameterisation

2.1 Governing parameters

In this study, the synthetic jet centreline velocity at orifice exit is given by [7]:

$$u(t) = u_{max} sin(\frac{2\pi t}{\tau} + \theta) \tag{1}$$

where u_{max}, t and τ represents the maximum velocity during the blowing cycle, time and period of the cycle, respectively. Further, the mean blowing velocity, $\bar{u}$, is used as a representative velocity throughout and is defined as

$$\bar{u} = \frac{1}{\tau}\int_0^{\tau/2} u(t)dt = \frac{1}{\tau}\int_0^{\tau/2} u_{max} sin(\frac{2\pi t}{\tau})\, dt = \frac{u_{max}}{\pi} \tag{2}$$

The momentum flow velocity U_0 is defined as [8]:

$$U_0 = \frac{\bar{u}\pi}{\sqrt{2}} \tag{3}$$

Three dimensionless parameters AR, Sr and Re are defined as [1]:

$$\mathrm{AR} = \frac{l}{d} \tag{4}$$

$$Sr = \frac{fd}{\bar{u}} = \frac{d}{L_o} \tag{5}$$

$$Re = \frac{\bar{u}d}{\nu} \tag{6}$$

while ν is the fluid kinematic viscosity, $f = 1/\tau$ is the actuation frequency, and L_o the stroke length, is defined as:

$$L_o = \frac{\bar{u}}{f} \tag{7}$$

Hence, based on above definition, an $AR = 10$ rectangular impinging synthetic jet at $Re = 550$, $Sr = 0.0117$, and $L_o = 0.0855m$ is investigated in this paper, while the $u_{max} = 26.85m/s$ and $\bar{u} = 8.55\ m/s$ were measured using hot-wire anemometry and calibrated in previous work [14,49].

2.2 Experimental setup and LF-PIV measurement

The experimental setup of rectangular impinging synthetic jet is schematically shown in Fig. 1. The synthetic jet actuator was forced by a Visaton SC 8N speaker, which was characterised by an 8Ω impedance with a rated power of 30W and its frequency range was $70 - 20000\ Hz$. The peak-to-peak voltage value of the upper amplitude limit was set as 15 and the actuator frequency was set as $f = 1/\tau = 100$Hz. A rectangle nozzle, with width $d = 1mm$ and length $l = 10mm$ ($AR = 10$), was manufactured by 3D printing with $0.1mm$ accuracy. The actuator was constituted by the speaker and an aluminium plate with the nozzle on its side. The actuator was directly mounted on a horizontal plate whose size is $300d \times 200d$, with the slot exits perpendicular to the impingement plate. The cavity has a volume of $1.85 \times 10^{-5}m^3$ and a neck length of $l_{neck} = 19.5$ mm. The impingement plate was located $24d$ from the orifice and has the same size as the plate where actuator mounted. In addition, those two plates were surrounded and sealed by four plexiglass such that uniform seeding could be achieved in such a "smoke box". Seeding particles (Pro Smoke Super particles $1\ \mu m$) were generated by a Martin MAGNUM 1200 smoke machine with a seeding density of around 1.0 particle per micro-lens (PPM). The measurement volume was illuminated with a double pulse Nd:YAG laser (500 mJ/pulse, 532nm, Litron), and the laser volume beam was formed using two cylindrical convex lens and two cylindrical concave lenses.

An in-house double frame light-field camera (6600×4400 pixels) [45] with a Micro-NIKKOR $200mm$ lens was applied to capture the measurement volume ($36 \times 22 \times 11d$), which located $1d$ away from the orifice centre. This in-house light-field camera was modified from a high-resolution camera (ImperX B6640) with a 520×360 micro-lens array precisely fixed near the sensor [44,45]. To achieve the best possible measurement resolution, the magnification factor was carefully adjusted to 1. The time interval between two image frames was 0.1 ms to ensure a maximum particle displacement of 64 pixels so as to comply with the one-quarter rule for three-dimensional cross-correlation. The laser, camera, and actuator were phase-locked to the driving signal at 20

equidistant phases by using a National Instruments NI-PXIe 1062Q data acquisition. 200 light-field image pairs were captured and processed for each phase by using single-camera LF-PIV.

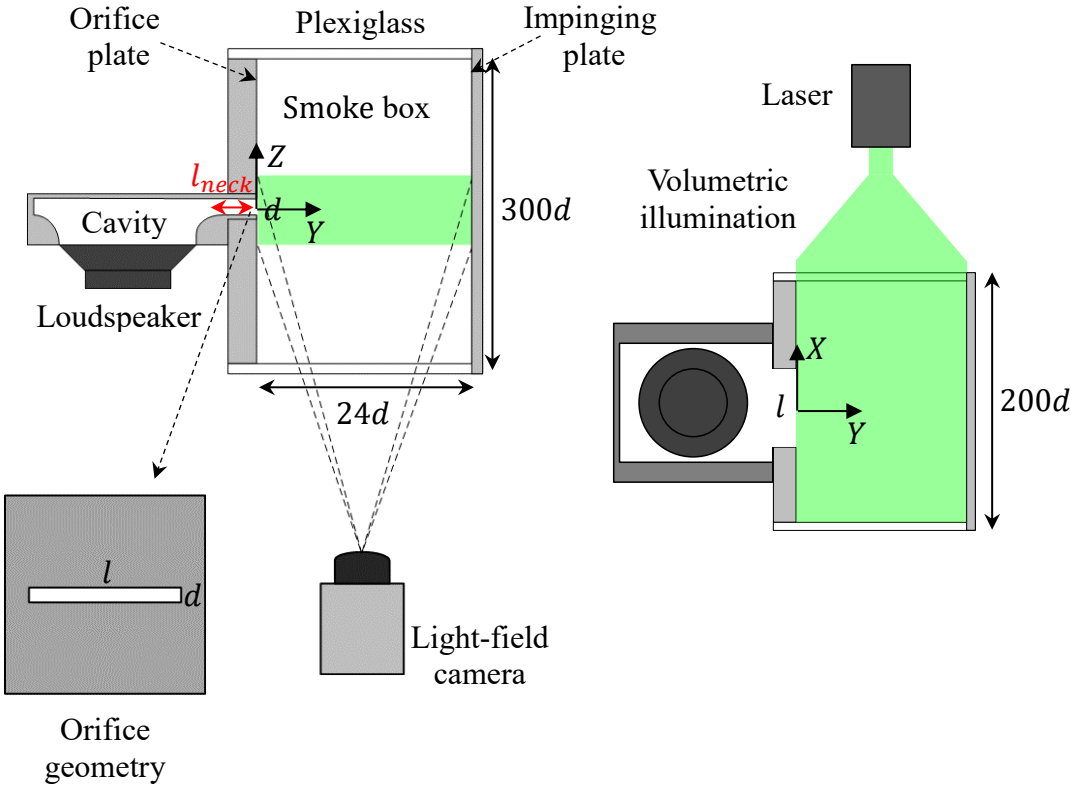

Fig. 1 Schematic of the rectangular impinging synthetic jet experimental setup.

A general flow chart for the framework of LF-PIV is shown in Fig. 2. An LF-PIV measurement consists of illuminating seeded flow and focusing the camera on the measured volume centre, which is in the same manner as in traditional 2D-PIV with the exception that the camera is a light-field camera. Following capturing raw light-field particle image pairs, a series of calibration images were acquired. In this step, a calibration board with dot pattern was linearly moved step by step, while the light-field camera recorded the images of that board. This procedure could be carried out before or after capturing raw particle images, as long as the optical settings of the camera remained unchanged. Then with these images, the calibration parameters of the light-field camera were calculated via a volumetric calibration method [50]. Pre-processing was implemented by subtracting the background noise from each raw light-field particle images, while the background noise image was generated by calculating the minimum value of each pixel in 100 image pairs. Then from each raw light-field particle image, 3D particle intensity volume was reconstructed via the DRT-MART reconstruction algorithm with 10 iterations [51]. The measurement volume was

reconstructed into $3200 \times 2150 \times 200$ voxel ($0.011 \times 0.011 \times 0.056$ mm^3/voxel). Instantaneous velocity fields were calculated by using three-dimensional multigrid cross-correlation with 50% overlap, the initial and final interrogation volumes were $256 \times 128 \times 32$ voxel and $128 \times 64 \times 16$ voxel respectively. So, each final velocity field has 83750 ($50 \times 67 \times 25$) velocity vectors with $\Delta_{X,Y,Z} = (0.704d, 0.352d, 0.224d)$ spacing between vectors. In each instantaneous velocity field, there are on average 4.1% spurious vectors detected by a $3 \times 3 \times 3$ median filter and replaced through linear interpolations. Reconstruction and cross-correlation process were paralleled by NVIDIA 1080Ti GPU units.

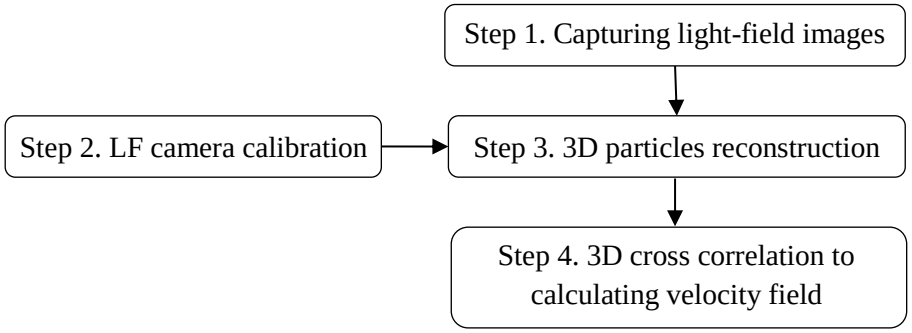

Fig. 2 Flow chart of single-camera light-field PIV

3 Results and Discussion

In this section, the experimental results are presented and discussed with detailed descriptions of 3D-3C velocity data. A convergence examination of second-order statistics has been performed. It is shown that the variation level of second-order statistics at the vortex core can be less than 10% of the average when the number of snapshots of the flow fields at the same phase is larger than 190. According to the conclusion in [53], such a result could meet the current study requirements and the number of snapshots per phase is sufficient for the mean flow.

3.1 Time-averaged results

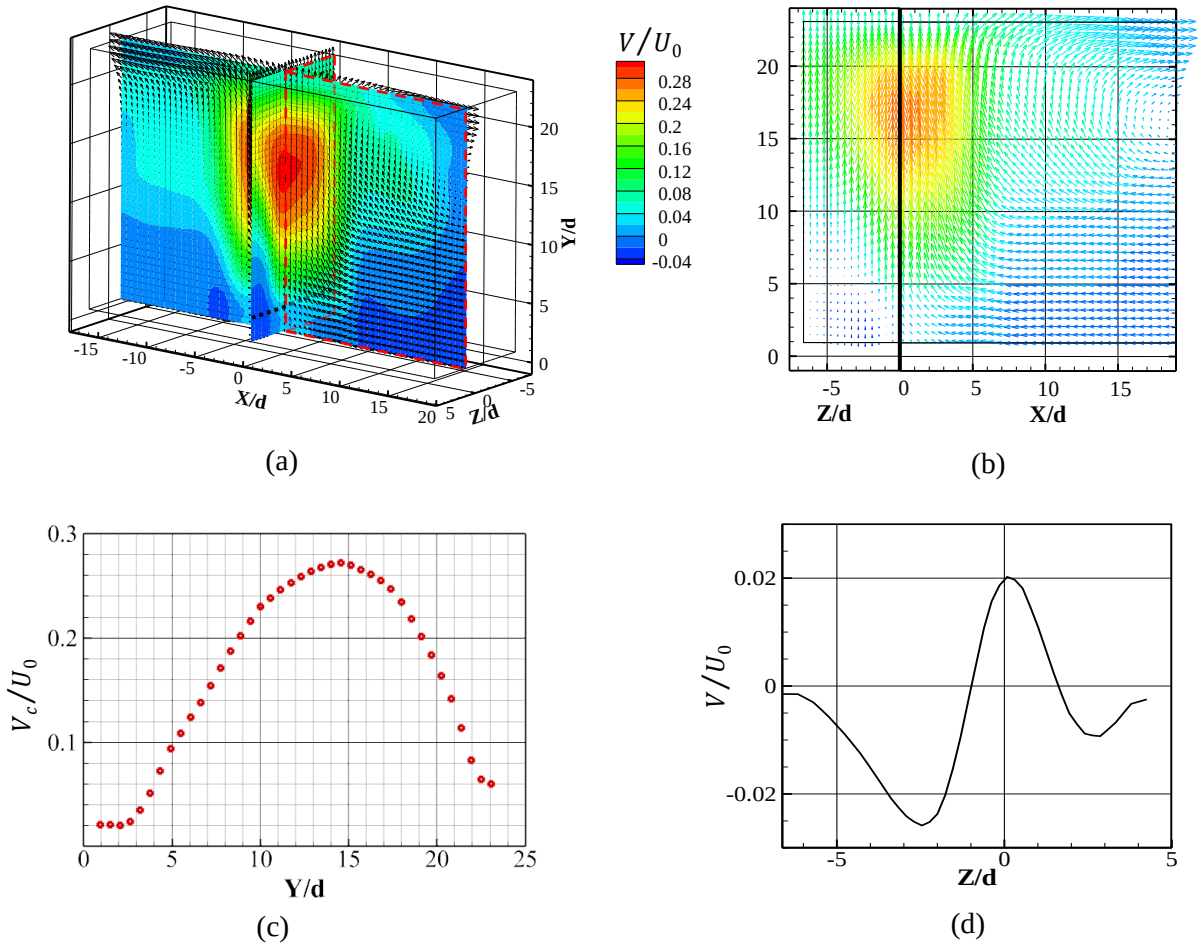

Fig. 3 Time averaged mean velocity vector field. Axial velocity V/U_0 maps in (a) 3D volume and (b) $Z/d = 0$ plane in $X - Y$ view and $X/d = 0$ plane in $X - Y$ view; (c) axial mean centre-line velocity $V_c(y)/U_0$ variation along Y-direction; (d) axial velocity V/U_0 profile along ($X = 0, Y = 2d, Z = -6.6d$ to $4.3d$), along the black dotted line in (a)

Figure 3(a) shows the nondimensionalised time-averaged axial velocity (V) distribution, which is used to extract the velocity distribution in $Z/d = 0$ and $X/d = 0$ planes (Fig. 3(b)). The variation of time-averaged axial centreline velocity $V_c(y)$ in the axial direction is plotted in Fig. 3(c), which shows that $V_c(y)$ reaches to zero near the orifice exit as expected by the fact that the jet is zero-net-mass-flux in nature. It is observed that the impingement plate affects the flow field up to $10d$ upstream, and the slope changes at approximately $10d$ upstream of the impingement plate. Figure 3(d) shows that the axial velocity V/U_0 profile along ($X = 0, Y = 2d, Z = -6.6d$ to $4.3d$) is asymmetric, which indicates that this impinging synthetic jet is asymmetric too. This is caused by an asymmetric design of the actuator, with the speaker mounted on a lateral side of the cavity rather

than on the side opposite to the orifice. Such asymmetry can have a clear influence on the evolution of the flow and some phenomena will be discussed later.

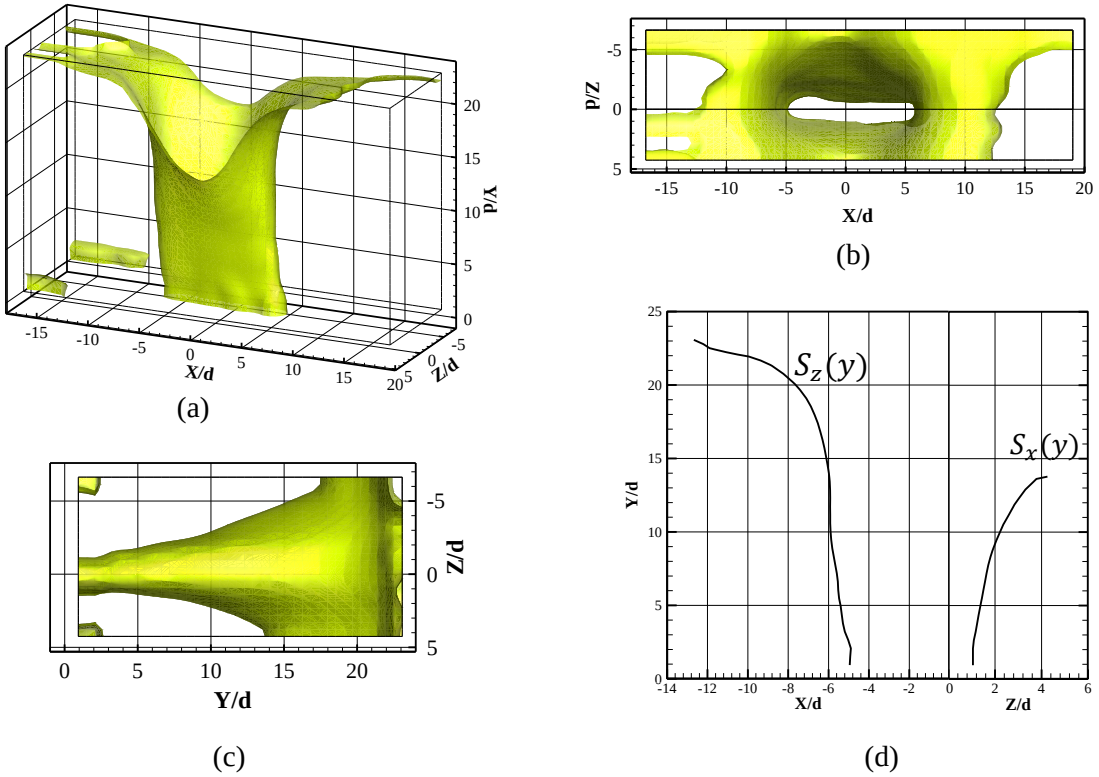

Fig. 4 Half-width surface $r_{1/2}(x, y, z) = 0$ shown in (a) 3D view; (b) top view; (c) side view; (d) the spine of half-width surface in $Z/d = 0$ plane $S_z(y)$, and in $X/d = 0$ plane $S_x(y)$.

Figures 4(a, b, c) show the half-width surface $r_{1/2}(x, y, z) = 0$, which is defined as the radial distance where the time-averaged axial velocity V decays to half its centreline value $V_c(y)$. The shape of this surface resembles a horn growing from a rectangle at the orifice to circle near the impingement plate. Figure 4(d) shows the spine of half-width surface $S_z(y)$ (in $Z/d = 0$ plane) and $S_x(y)$ (in $X/d = 0$ plane). $S_z(y)$ is found to increase slowly from orifice to the position approximately $10d$ away from the impingement plate, then increases rapidly. This shows the effect of impinging plate on jet behaviour. However, $S_x(y)$ is found to increase smoothly from the orifice ($1d$) till boundary of the study region. As shown in the figure, $S_x(y)$ grows faster than $S_z(y)$. This indicates that there is a well-known 'axis switching' phenomenon [54,55]. At the orifice position, the jet width $S_z(Y/d = 0)$ and $S_x(Y/d = 0)$ is slightly smaller than $l/2$ and $d/2$ because of the recirculation flow and the vena contracta phenomenon that develops along the orifice edge.

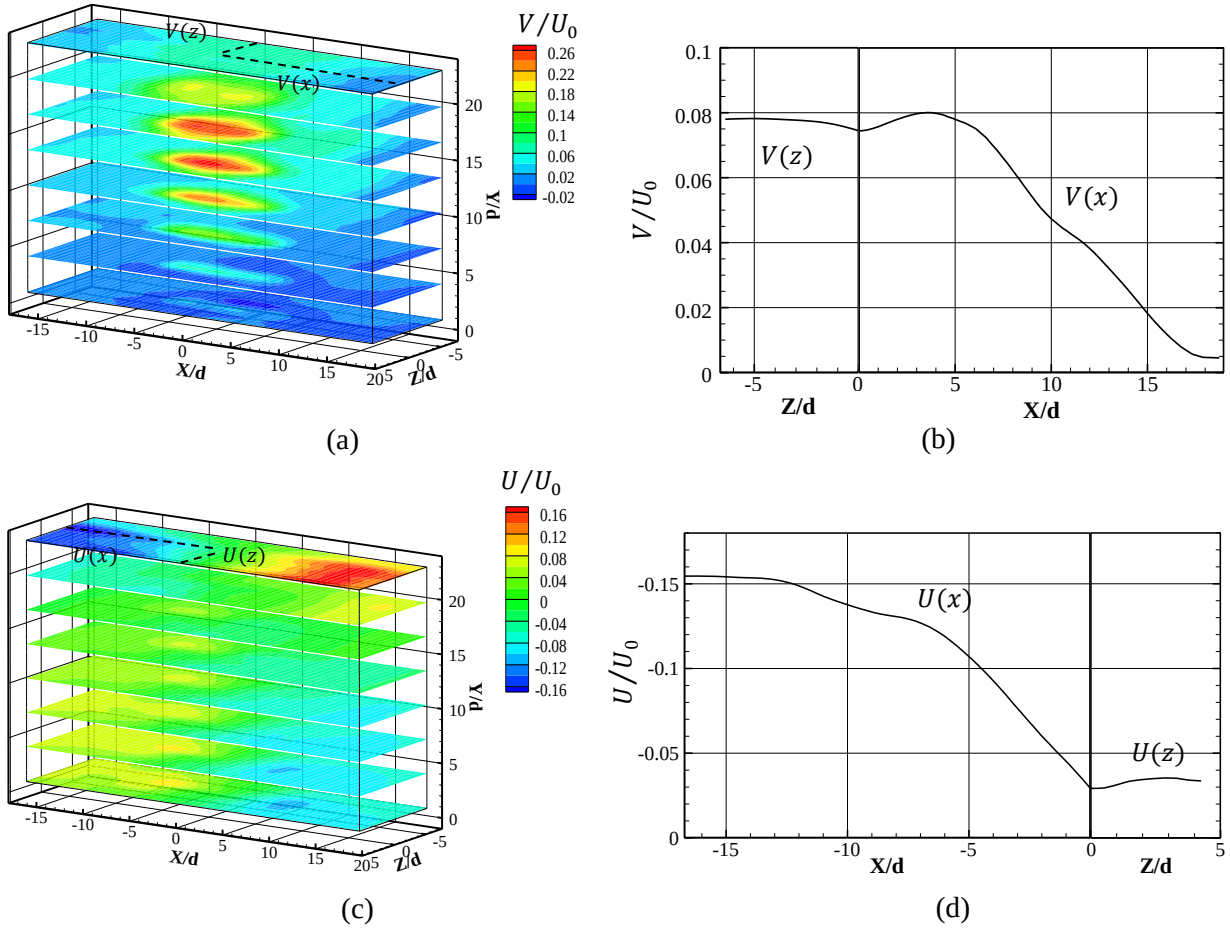

Fig. 5 (a) 3D contours of time-averaged velocity component V; (b) V profile along ($X = 0$ to $18.7d$, $Y = 23d$, $Z = 0$), $V(x)$, and V profile along ($X = 0$, $Y = 23d$, $Z = -6.2d$ to 0), $V(z)$, (along the two black dotted line in (a)); (c) 3D contours of time-averaged velocity component U; (d) U profile along ($X = -16.7d$ to 0, $Y = 23d$, $Z = 0$), and U profile along ($X = 0$, $Y = 23d$, $Z = -4.3d$ to 0), $U(x)$, (along the two black dotted line in (c))

Flow field behaviour near the impingement plate is characterised via the time-averaged axial velocity components. Figures 5 (a) and (c) show the 3D contours for V and U, respectively. Figure 5(b) plots the V profile along ($X = 0$ to $18.7d$, $Y = 23d$, $Z = 0$), $V(x)$, and V profile along ($X = 0$, $Y = 23d$, $Z = -6.2d$ to 0), $V(z)$. It is clear that there are local minima along the jet axis for both $V(x)$ and $V(z)$. For $V(x)$ profile, the absolute maximum is detected at $X = 3d$, and after that, the value starts to decrease monotonically. Nevertheless, $V(z)$ decreases slowly and then shows a minimum value near the centreline. This can be ascribed to the flow field topology. Because of the axis switching phenomenon, the extent of vortex ring from the synthetic jet is longer along the Z-axis compared to the X-axis. According to the previous result [35], the radial velocity along the

impingement plate has two main components: sweeping vortex and wall jet generated by the impinging trailing jet. In this study, due to the limited measurement volume, a fully developed wall jet region is not included. In Fig. 5(d), the $U(x)$ profile along ($X = -16.7d$ to 0, $Y = 23d$, $Z = 0$) shows a minimum value near the centreline, and decreases rapidly in $0 > X \geq -7d$, which is ascribed to the wall jet generated by the impinging trailing jet. Then $U(x)$ decreases slowly in $-16.7d \leq X \leq -13d$, while it reaches a peak plateau at $X = -13d$ because of the sweeping vortex ring. Besides, W/U_0 varies in a relatively small range ($-0.005 < W/U_0 < 0.005$), when comparing the range of U/U_0 and V/U_0, which imposes a common challenging situation for data process. Similar to other cross-correlation based PIV methods, LF-PIV also suffers from the conflict between dynamic range and seeding density. The initial and final interrogation volumes were carefully selected to ensure the one-quarter-rule for U and V, while such volume size may be slightly too large for W. However, if an even smaller volume (in Z-direction) was selected, with current particle density which is fundamentally limited by MLA resolution [45], there won't be enough tracer particles for a statistically meaningful result. As such, 3D contours for W are not presented here.

3.2 Phase-averaged results

The formation and evolution of 3D flow structures are depicted by phase-averaged velocity and λ_{ci}-criterion. The phase-averaged velocity is the average in any spatial point for a fixed phase t/τ in the synthetic jet generation cycle (In this study 20 equidistant phases were acquired, so the range of t/τ is from $0/20$ to $19/20$). Several phases are selected from ejection phases ($t/\tau = 0/20$ to $t/\tau = 9/20$) and suction phases ($t/\tau = 10/20$ to $t/\tau = 19/20$) to present the synthetic jet cycle.

Figure 6 shows the phase-averaged contour of nondimensionalised velocity component $\langle v \rangle$ in $Z = 0$ and $X = 0$ plane. As can be seen from the figure, the ejection phase starts at $t/\tau = 0/20$, the vortex ring is completely formed at $t/\tau = 2/20$, and the synthetic jet starts to impinge on the plate at $t/\tau = 7/20$. The maximum of $\langle v \rangle$ is presented at $t/\tau = 2/20$ on the centreline of the vortex ring core. At $t/\tau = 2/20$ to $t/\tau = 4/20$, there are clear signs of higher negative velocity $\langle v \rangle$ in the $X = 0$ plane compared to $Z = 0$ plane at the outer periphery of the vortex ring caused by the roll-up structure.

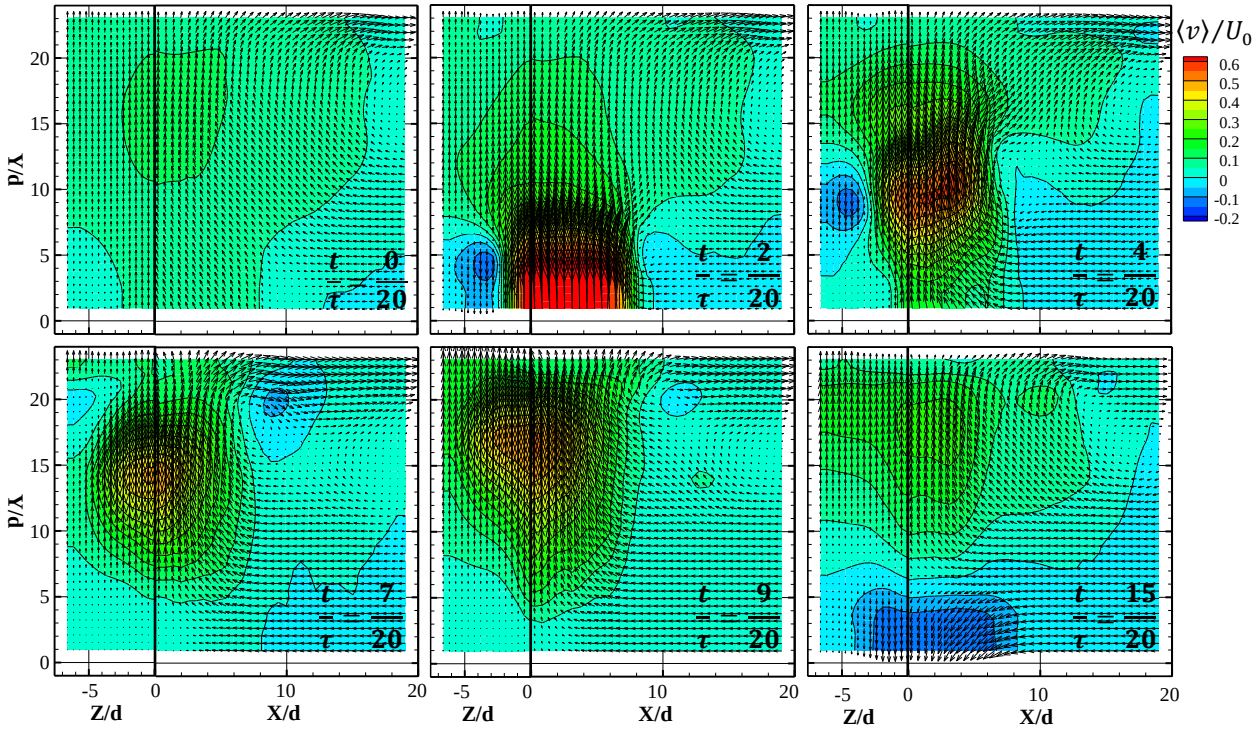

Fig. 6 The nondimensionalised phase-averaged $\langle v \rangle$ distribution on $X = 0$ (left) and $Z = 0$ (right) plane

During the suction phase of the synthetic jet, the flow is characterised by a saddle point [16], where the fluid velocity at this point is equal to zero. The behaviour of the nondimensionalised distance between the saddle point and orifice plate (D_{so}) is depicted in Fig. 7. The position of a saddle point is determined through the detection of the point characterised by zero phase-averaged velocity ($\langle u \rangle = 0, \langle v \rangle = 0, \langle w \rangle = 0$) inside the half-width surface shown in Fig. 4(b). At the beginning of the suction phase, D_{so} increases with t/τ increasing up to $t/\tau = 15/20$, at which point in time, $\langle v \rangle$ attains negative maxima near the orifice jet axis centreline. Then D_{so} starts to decrease as t/τ increases, which is ascribed to the gradually weakened external force. This is consistent with previous results [35], which shows that the device configuration has a great influence on the saddle point behaviour. The two parallel plates (the orifice plate, and impingement plate) can confine the flow field region of the synthetic jet, however, such a confinement influence is less significant in the region near the nozzle in the current case. At suction phases such as $t/\tau = 15/20$ in Fig. 6, strong flow separation is noticed occurring along the iso-surface of $\langle v \rangle = 0$. The boundary position and geometry of such a flow separation at different suction phases are dominated by the interaction of suction strength and entraining ability of the roll-up vortex ring and the sweeping vortex.

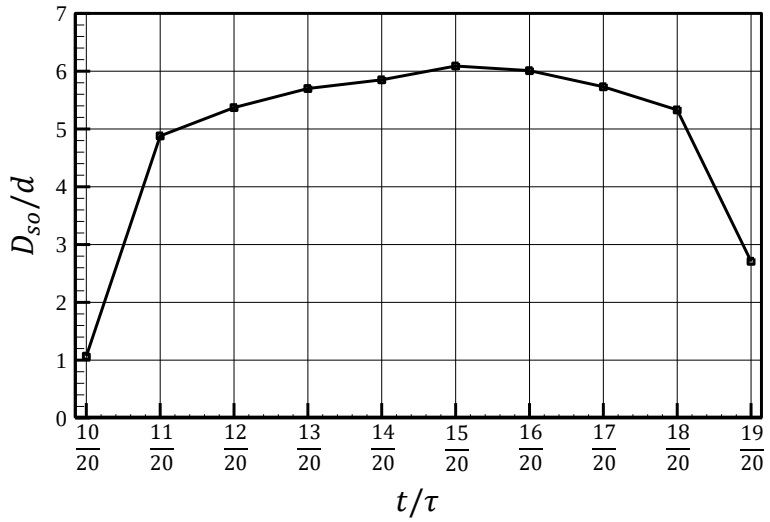

Fig. 7 The saddle point behaviour at suck phases

The streamwise evolution of three-dimensional vortical structures is characterised through the phase-averaged λ_{ci}. The λ_{ci}-criterion method is based on the idea that the velocity gradient tensor $\boldsymbol{D} = \boldsymbol{\nabla u}$ can be decomposed in Cartesian coordinates as [52],

$$\boldsymbol{D} \equiv \left[d_{i,j}\right] = [\boldsymbol{v_r} \quad \boldsymbol{v_{cr}} \quad \boldsymbol{v_{ci}}] \begin{bmatrix} \lambda_r & & \\ & \lambda_{cr} & \lambda_{ci} \\ & -\lambda_{ci} & \lambda_{cr} \end{bmatrix} [\boldsymbol{v_r} \quad \boldsymbol{v_{cr}} \quad \boldsymbol{v_{ci}}]^{-1} \tag{15}$$

where the λ_r is the real eigenvalue with the corresponding eigenvector $\boldsymbol{v_r}$, and $\lambda_{cr} \pm i\lambda_{ci}$ are the complex conjugate pair of complex eigenvalues with complex eigenvectors $\boldsymbol{v_{cr}} \pm i\boldsymbol{v_{ci}}$. The variation of the flow structures is examined with three typical thresholds of λ_{ci} ($\lambda_{ci} = 0.0012$, 0.013 and 0.0375). Though the three representatives, the flow structures with different vortex strengths can be distinguished. As Fig. 8 shows, the main vortex ring, which is identified by $\lambda_{ci} = 0.0375$, is visible at $t/\tau = 2/20$ for the first time. Then the vortex ring grows and forms its shape at $t/\tau = 4/20$. From $t/\tau = 4/20$ to $t/\tau = 6/20$, the vortex ring rolls up and propagates upstream to the impingement plate with the vortex ring geometry evolution caused by the axis switching (black dash line). Also starting from $t/\tau = 5/20$, the asymmetric development rate between the left and right parts of the vortex ring becomes apparent. This is due to the asymmetric velocity distribution caused by the asymmetric nozzle design, and will be further discussed in Fig. 9. The right part of the vortex ring starts to impinge the plate approximately at $t/\tau = 7/20$ and the whole vortex ring fully hits the plate at $t/\tau = 8/20$. Then vortex ring breaks and develops along the plate. It evolves into the sweeping vortex (green circle) at around $t/\tau = 12/20$. The sweeping vortex exists until $t/\tau = 6/20$ of the next period. The trailing jet also starts to impinge the plate at $t/\tau =$

$12/20$, which fully disappears at $t/\tau = 19/20$. Moreover, due to the limited measurement volume, the entire recirculating vortex cannot be measured and presented. While the previous work [33] indicates that following the development of sweeping vortex, a strong flow separation, that leads the sweeping vortex to move away from the impingement plate and to evolve into part of the recirculating vortex, could be observed. According to this, the vortex structures in the yellow circle could be inferred as part of the recirculating vortex. The vortex structures show up around a counter-current flow in the streamwise direction when comparing the Fig. 8 and the vector distribution from Fig. 6. It is worth notice that the iso-surface generated from LF-PIV results is not perfectly smooth in the following figures. Generally, it is caused by its limited ability in resolving complex structures. Based on our current in-house light-field camera, it is impossible to achieve a refined measurement result that is in the same quality as TR 2D-PIV [31] or other multi-camera PIV methods, when the resolution of camera is at the same level. But the bearable sacrifice in resolution makes LF-PIV able to produce a relatively convenient whole-field snapshot with essential details.

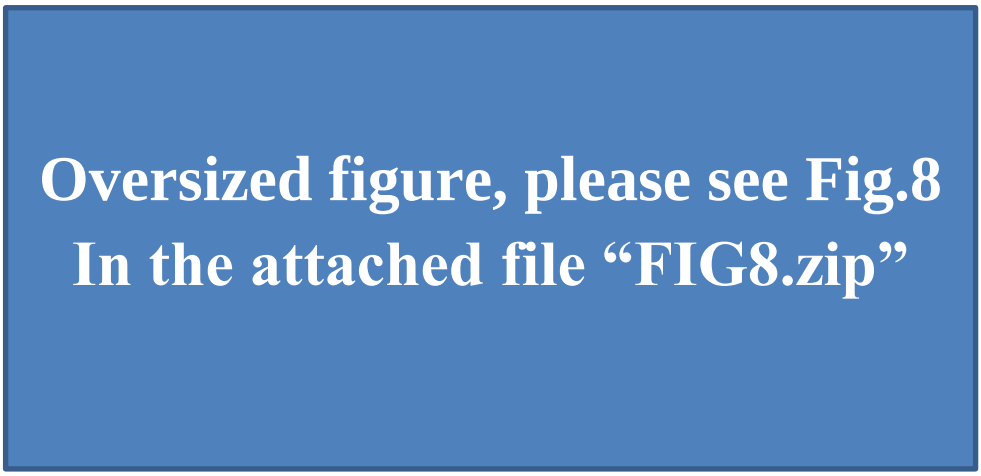

Fig. 8 Streamwise evolution of iso-surfaces of phase-averaged λ_{ci} (blue: $\lambda_{ci} = 0.0012$, green: $\lambda_{ci} = 0.013$, orange: $\lambda_{ci} = 0.0375$). SV-I, SV-II, and AV denote streamwise vortex I, streamwise vortex II, and arc-like vortex. The green circles point out the structures belonging to

the sweeping vortex and the orange circle point out the structures belonging to the recirculating vortex

Besides the evolution of main vortex ring, other different vortical structures along with the main vortex ring are also observed. According to the previous research [29–31], these structures have been named as streamwise vortex I (SV-I), streamwise vortex II (SV-II), and arc-like vortex (AV). The SV-I is paired up in the major-axis direction and formed aligned with the corner regions of the rectangle orifice. As shown in Figs. 8 and 9, SV-I is observed at $t/\tau = 3/20$ and moves downstream along with the main vortex ring. As the evolution of main vortex ring, the arc-like vortical structures can be observed. AV fully develops at $t/\tau = 4/20$ and starts to hit the plate at $t/\tau = 5/20$. Also, it is worth noting that some vortical structures, which seem to be related to the formation of AV, can be found at $t/\tau = 2/20$ and $t/\tau = 3/20$ around the main vortex ring. The strong streamwise components of the AV, which is denoted as SV-II, can be recognised clearly at $t/\tau = 4/20$.

Oversized figure, please see Fig.9
In the attached file "FIG9.pptx"

Fig. 9 Front and side views of iso-surfaces of phase-averaged λ_{ci} (blue: $\lambda_{ci} = 0.0012$, green: $\lambda_{ci} = 0.013$, orange: $\lambda_{ci} = 0.0375$) at $t/\tau = 3/20$ to $t/\tau = 6/20$.

From the Figs. 8 and 9, it is clear that the main characterisation of vortical structures of this rectangle orifice impinging synthetic jet can be detected, while it is also notable that these vortical structures are slightly different from the structures of typical rectangle orifice synthetic jet [29,31]. SV-I seems to merge together as one single elongated vortical structure instead of two pairs of the inclined elongated structures. This drop in resolution is similar to other measurement results of LF-PIV [47] and may be due to the limited resolution of single-camera LF-PIV near the focal plane [45,56,57], so the details of vortical structure cannot be resolved. As for SV-II and AV, in this paper, these two kind structures can be seen in $Z < 0$ volume while the symmetrical parts in $Z > 0$ volume are absent. However, from the side view in Fig. 9, some structures belonging to SV-II and AV can be found in the right edge of the volume. Hence, the absence of symmetrical parts of SV-II and AV is caused by the limited measurement volume. Moreover, the main vortex ring is not closed. From Figs. 8 and 9, part of the vortex ring in $Z < 0$ volume is absent. As Fig. 3(d) shows, velocity near the orifice is asymmetric and velocity in $Z < 0$ range is larger. The asymmetric design of the actuator (the speaker mounted on a lateral side of the cavity rather than on the side opposite to the orifice) is probably the reason for this clear influence. This is quite an interesting problem and further investigation needs to be done for more evidence. Besides, according to Figs. 8 and 9, it is notable that the right part ($X > 0$) of the main vortex ring along the major axis plane ($X - Y$ plane) moves faster than another part. A possible reason could be that the remaining sweeping vortex and structures belonging to the recirculating vortex (the red dash box, Fig. 10) on the right side are stronger. As Fig. 10 shows, the normalised nondimensionalised vorticity component $\langle \omega_z \rangle$ on $Z = 0$ plane indicates that the stronger vortical structures push the right part of the main vortex ring to move faster. Also, the asymmetric actuator design makes the velocity component $\langle V \rangle$ in the green dash box lager than that of the symmetric side ($X < 0$). These two factors jointly affect the main vortex ring which results in its right part moving faster than the left one. In addition, a pair of secondary counter-rotating vortices is inside the main vortex ring on the major axis plane, which is caused by the large space between the edge vortices (by large AR) [28]. This secondary structure is generated by the secondary bending of the vortex ring.

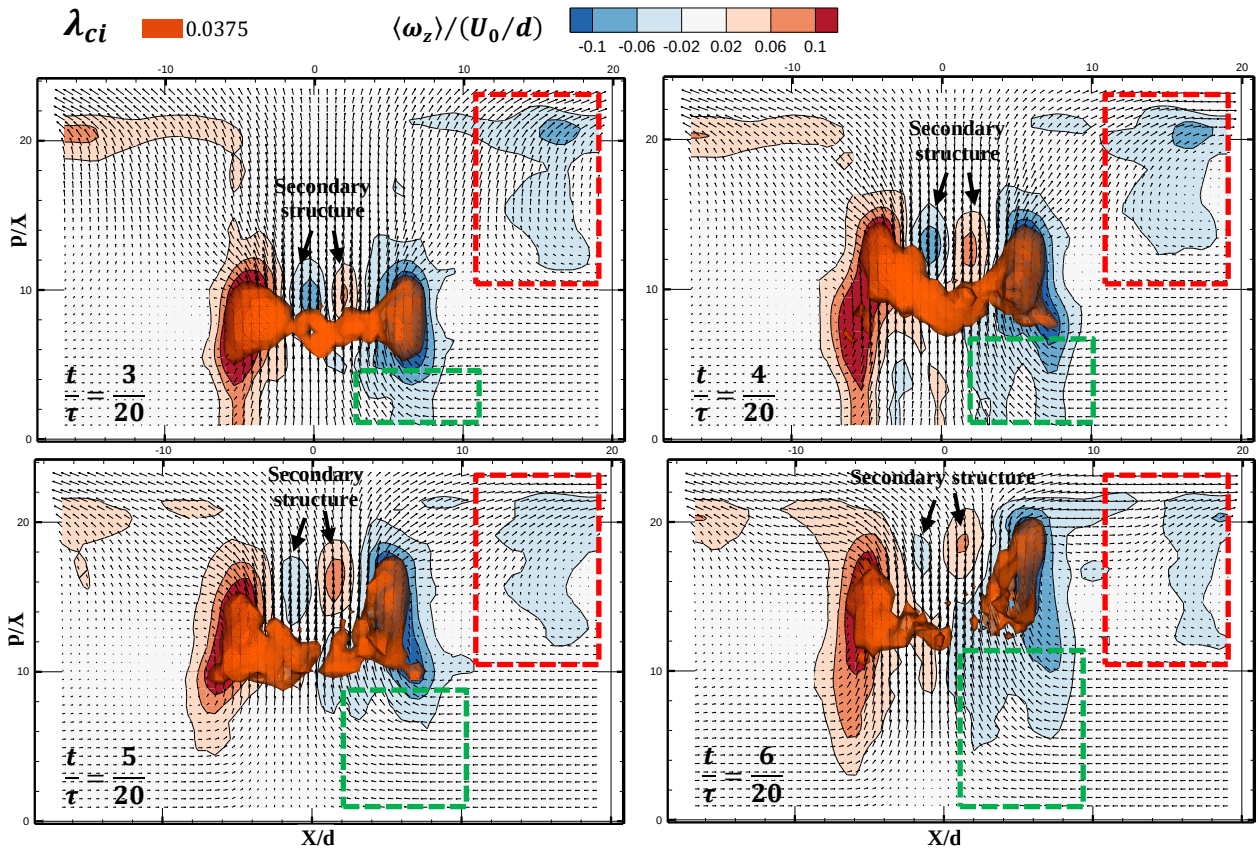

Fig. 10 The nondimensionalised vorticity component $\langle\omega_z\rangle$ distribution on $Z = 0$ plane from $t/\tau = 3/20$ to $t/\tau = 6/20$. The red dash line denotes the vortical structures belonging to the sweeping vortex and part of the recirculating vortex

Figure 11 presents the main vortex ring structure at $t/\tau = 4/20$ in the 3D, front and side view. As a result of the Biot-Savart mechanism [58], the vortex cores at the major axis plane ($X - Y$ plane) initially move faster than those in the minor axis ($Y - Z$ plane), owing to the higher orifice curvature. Then they approach each other and reach a minimum distance. The black dash curves in Fig. 11 are trying to briefly represent the vortex ring core geometry in each view. It is conspicuous that the edges of the vortex ring move faster than the centre in the front view, and the middle portion moves faster than the sides of the vortex ring in the side view. That is the early stage of the axis switching. However, due to the presence of the impinging plate, the main vortex ring cannot finish the rest stages of axis switching. The rest stages of axis switching mean that the vortex cores at minor axis move away from each other until a maximum distance is reached. Besides, as the side views at $t/\tau = 5/20$ and $t/\tau = 6/20$ of Fig. 9 show, the main vortex ring spreads along the minor

axis and stretches beyond the edge of the measured volume in the Z-axis. Hence, the first vortex ring axis switching is not fully presented here.

Oversized figure, please see Fig.11 In the attached file "FIG11.pptx"

Fig. 11 Iso-surfaces of phase-averaged λ_{ci} (orange: $\lambda_{ci} = 0.0375$, red: $\lambda_{ci} = 0.0480$) at $t/\tau = 4/20$. (a) 3D view; (b) side view; (c) front view.

4 Conclusion

The three-dimensional flow structure of a rectangle orifice impinging synthetic jet was investigated experimentally using the phase-locked single-camera LF-PIV. At the beginning of ejection phases, the vortex ring starts at the edges of the orifice. Then the vortex ring goes through a process of growing downstream and propagating to the impingement plate. During the process, the vortex ring geometry evolves from a rectangle with a similar size as the orifice into another rectangle with opposite length-width due to axis-switching. At ejection phases, near the orifice field, flow features

of the impinging synthetic jet are dominated by the main vortex ring. At suction phases, the interaction of the vortex ring and strong flow separation which is represented through the saddle point takes the primary effect on the flow characteristics. One part of the flow is drawn to the orifice by the suction negative pressure while the other part is rolled up with vortex ring and sweeping vortex. After the vortex ring hitting the impingement plate, it forms a sweeping vortex which plays a major role in the flow field near the impingement plate.

The complicated 3D vortical structures of the rectangle orifice synthetic jet are resolved, including axis switching of the main vortex ring, the formation of the streamwise vortex and the arc-like vortex. Some vortex structures belonging to the large recirculating flow between the impinging plate and orifice plate are observed. While LF-PIV cannot provide perfectly smooth vortex iso-surface or maintain a high resolution of flow statistics in the focal plane of the measured volume, it is shown that this volumetric flow diagnostic technique could be a valuable tool in resolving complex structures and presenting a whole-flow-field snapshot.

Acknowledgements

The authors are grateful to Southampton University for facilitating the experiments. This work is supported by the National Natural Science Foundation of China (Grant No.11472175, No.11772197) and the Royal Society Travel Grant.

References

[1] A. Glezer, M. Amitay, Synthetic jets, Annu. Rev. Fluid Mech. 34 (2002) 503–529.

[2] D.P. Rizzetta, M.R. Visbal, M.J. Stanek, Numerical investigation of synthetic-jet flowfields, AIAA J. 37 (1999) 919–927.

[3] R. Byrganhalli, R. Mittal, F. Najjar, Study of three-dimensional synthetic jet flowfields using direct-numerical simulation, in: 42nd AIAA Aerosp. Sci. Meet. Exhib., 2004: p. 91.

[4] H. Tang, S. Zhong, 2D numerical study of circular synthetic jets in quiescent flows, Aeronaut. J. (2005). https://doi.org/10.1017/S0001924000000592.

[5] B.R. Ravi, R. Mittal, Numerical study of large aspect-ratio synthetic jets, in: Collect. Tech. Pap. - 44th AIAA Aerosp. Sci. Meet., 2006. https://doi.org/10.2514/6.2006-315.

[6] Q. Xia, S. Lei, J. Ma, S. Zhong, Numerical study of circular synthetic jets at low Reynolds numbers, Int. J. Heat Fluid Flow. 50 (2014) 456–466.

[7] B.L. Smith, A. Glezer, The formation and evolution of synthetic jets, Phys. Fluids. 10 (1998) 2281–2297.

[8] J.E. Cater, J. Soria, The evolution of round zero-net-mass-flux jets, J. Fluid Mech. 472 (2002) 167–200.

[9] J.M. Shuster, D.R. Smith, Experimental study of the formation and scaling of a round synthetic jet, Phys. Fluids. 19 (2007) 45109.

[10] J. Dandois, E. Garnier, P. Sagaut, Numerical simulation of active separation control by a synthetic jet, J. Fluid Mech. 574 (2007) 25–58.

[11] N.A. Buchmann, C. Atkinson, J. Soria, Influence of ZNMF jet flow control on the spatio-temporal flow structure over a NACA-0015 airfoil, Exp. Fluids. 54 (2013) 1485.

[12] R. Rathnasingham, K.S. Breuer, Active control of turbulent boundary layers, J. Fluid Mech. 495 (2003) 209–233.

[13] J. Canton, R. Örlü, C. Chin, N. Hutchins, J. Monty, P. Schlatter, On large-scale friction control in turbulent wall flow in low Reynolds number channels, Flow, Turbul. Combust. 97 (2016) 811–827.

[14] T. Berk, N. Hutchins, I. Marusic, B. Ganapathisubramani, Trajectory of a synthetic jet issuing into high-Reynolds-number turbulent boundary layers, J. Fluid Mech. (2018). https://doi.org/10.1017/jfm.2018.734.

[15] R. Mittal, P. Rampunggoon, On the virtual aeroshaping effect of synthetic jets, Phys. Fluids. 14 (2002) 1533–1536.

[16] B.L. Smith, A. Glezer, Jet vectoring using synthetic jets, J. Fluid Mech. 458 (2002) 1–34.

[17] Z.-B. Luo, Z.-X. Xia, The mechanism of jet vectoring using synthetic jet actuators, Mod. Phys. Lett. B. 19 (2005) 1619–1622.

[18] T. Persoons, T.S. O'Donovan, D.B. Murray, Heat transfer in adjacent interacting impinging synthetic jets, in: ASME 2009 Heat Transf. Summer Conf. Collocated with InterPACK09 3rd Energy Sustain. Conf., 2009: pp. 955–962.

[19] P. Valiorgue, T. Persoons, A. McGuinn, D.B. Murray, Heat transfer mechanisms in an impinging synthetic jet for a small jet-to-surface spacing, Exp. Therm. Fluid Sci. 33 (2009) 597–603.

[20] M. Chaudhari, B. Puranik, A. Agrawal, Heat transfer characteristics of synthetic jet impingement cooling, Int. J. Heat Mass Transf. 53 (2010) 1057–1069. https://doi.org/10.1016/j.ijheatmasstransfer.2009.11.005.

[21] C.S. Greco, A. Ianiro, G. Cardone, Time and phase average heat transfer in single and twin circular synthetic impinging air jets, Int. J. Heat Mass Transf. 73 (2014) 776–788.

[22] M. Mueller, L. Bernal, R. Moran, P. Washabaugh, B. Parviz, T.-K. Chou, C. Zhang, K. Najafi, Thrust performance of micromachined synthetic jets, in: Fluids 2000 Conf. Exhib., 2000: p. 2404.

[23] A.G. Athanassiadis, D.P. Hart, Effects of multijet coupling on propulsive performance in underwater pulsed jets, Phys. Rev. Fluids. (2016). https://doi.org/10.1103/physrevfluids.1.034501.

[24] S. Zhong, M. Jabbal, H. Tang, L. Garcillan, F. Guo, N. Wood, C. Warsop, Towards the design of synthetic-jet actuators for full-scale flight conditions, Flow, Turbul. Combust. 78 (2007) 283–307.

[25] B.L. Smith, G.W. Swift, A comparison between synthetic jets and continuous jets, Exp. Fluids. 34 (2003) 467–472.

[26] M. Amitay, F. Cannelle, Evolution of finite span synthetic jets, Phys. Fluids. (2006). https://doi.org/10.1063/1.2196093.

[27] T. Van Buren, E. Whalen, M. Amitay, Vortex formation of a finite-span synthetic jet: High Reynolds numbers, Phys. Fluids. (2014). https://doi.org/10.1063/1.4859895.

[28] T. Van Buren, E. Whalen, M. Amitay, Vortex formation of a finite-span synthetic jet: Effect of rectangular orifice geometry, J. Fluid Mech. (2014). https://doi.org/10.1017/jfm.2014.77.

[29] L. Wang, L.-H. Feng, J.-J. Wang, T. Li, Evolution of low-aspect-ratio rectangular synthetic jets in a quiescent environment, Exp. Fluids. 59 (2018) 91.

[30] L. Wang, L.-H. Feng, J.-J. Wang, T. Li, Parameter influence on the evolution of low-aspect-ratio rectangular synthetic jets, J. Vis. 21 (2018) 105–115.

[31] L. Wang, L.-H. Feng, Y. Xu, Laminar-to-transitional evolution of three-dimensional vortical structures in a low-aspect-ratio rectangular synthetic jet, Exp. Therm. Fluid Sci. 104 (2019) 129–140.

[32] A. Pavlova, M. Amitay, Electronic cooling using synthetic jet impingement, (2006).

[33] F. Bazdidi-Tehrani, M. Karami, M. Jahromi, Unsteady flow and heat transfer analysis of an impinging synthetic jet, Heat Mass Transf. Und Stoffuebertragung. (2011). https://doi.org/10.1007/s00231-011-0801-0.

[34] A. McGuinn, R. Farrelly, T. Persoons, D.B. Murray, Flow regime characterisation of an impinging axisymmetric synthetic jet, Exp. Therm. Fluid Sci. 47 (2013) 241–251.

[35] C.S. Greco, G. Cardone, J. Soria, On the behaviour of impinging zero-net-mass-flux jets, J. Fluid Mech. 810 (2017) 25–59.

[36] Y. Xu, J.-J. Wang, Digital particle image velocimetry study on parameter influence on the behavior of impinging synthetic jets, Exp. Therm. Fluid Sci. 100 (2019) 11–32. https://doi.org/10.1016/j.expthermflusci.2018.08.024.

[37] M. Chaudhari, B. Puranik, A. Agrawal, Effect of orifice shape in synthetic jet based impingement cooling, Exp. Therm. Fluid Sci. 34 (2010) 246–256.

[38] T. Van Buren, M. Amitay, Comparison between finite-span steady and synthetic jets issued into a quiescent fluid, Exp. Therm. Fluid Sci. 75 (2016) 16–24. https://doi.org/10.1016/j.expthermflusci.2016.01.014.

[39] X. He, J.A. Lustbader, M. Arik, R. Sharma, Heat transfer characteristics of impinging steady and synthetic jets over vertical flat surface, Int. J. Heat Mass Transf. 80 (2015) 825–834.

[40] C.Y.Y. Lee, M.L. Woyciekoski, J.B. Copetti, Experimental study of synthetic jets with rectangular orifice for electronic cooling, Exp. Therm. Fluid Sci. 78 (2016) 242–248.

[41] E. Fanning, T. Persoons, D.B. Murray, Heat transfer and flow characteristics of a pair of adjacent impinging synthetic jets, Int. J. Heat Fluid Flow. 54 (2015) 153–166.

[42] O. Ghaffari, S.A. Solovitz, M. Arik, An investigation into flow and heat transfer for a slot impinging synthetic jet, Int. J. Heat Mass Transf. 100 (2016) 634–645.

[43] T.W. Fahringer, K.P. Lynch, B.S. Thurow, Volumetric particle image velocimetry with a single plenoptic camera, Meas. Sci. Technol. 26 (2015) 115201.

[44] S. Shi, J. Ding, C. Atkinson, J. Soria, T.H. New, A detailed comparison of single-camera light-field PIV and tomographic PIV, Exp. Fluids. 59 (2018) 46.

[45] S. Shi, J. Wang, J. Ding, Z. Zhao, T.H. New, Parametric study on light field volumetric particle image velocimetry, Flow Meas. Instrum. 49 (2016) 70–88.

[46] K.C. Johnson, B.S. Thurow, T. Kim, G. Blois, K.T. Christensen, Volumetric velocity measurements in the wake of a hemispherical roughness element, AIAA J. (2017) 2158–2173.

[47] Z. Zhao, A.-J. Buchner, C. Atkinson, S. Shi, J. Soria, Volumetric measurements of a self-similar adverse pressure gradient turbulent boundary layer using single-camera light-field particle image velocimetry, Exp. Fluids. 60 (2019) 141.

[48] W. Kevin, R. Berdon, J. Buchholz, K. Johnson, B.S. Thurow, Characterization and Manipulation of Vorticity Transport On a Rolling Wing, in: AIAA Scitech 2019 Forum, 2019: p. 2326.

[49] T. Berk, G. Gomit, B. Ganapathisubramani, Vectoring of parallel synthetic jets: A parametric study, J. Fluid Mech. (2016). https://doi.org/10.1017/jfm.2016.559.

[50] S. Shi, J. Ding, T.H. New, Y. Liu, H. Zhang, Volumetric calibration enhancements for single-camera light-field PIV, Exp. Fluids. 60 (2019) 21.

[51] S. Shi, J. Ding, T.H. New, J. Soria, Light-field camera-based 3D volumetric particle image velocimetry with dense ray tracing reconstruction technique, Exp. Fluids. 58 (2017) 78.

[52] J. Zhou, R.J. Adrian, S. Balachandar, T.M. Kendall, Mechanisms for generating coherent packets of hairpin vortices in channel flow, J. Fluid Mech. 387 (1999) 353–396.

[53] J.I. Cardesa, T.B. Nickels, J.R. Dawson, 2D PIV measurements in the near field of grid turbulence using stitched fields from multiple cameras, Exp. Fluids. 52 (2012) 1611–1627.

[54] M.R. Dhanak, B. de Bernardinis, The evolution of an elliptic vortex ring, J. Fluid Mech. 109 (1981) 189–216.

[55] K.B.M.Q. Zaman, Axis switching and spreading of an asymmetric jet: the role of coherent structure dynamics, J. Fluid Mech. 316 (1996) 1–27. https://doi.org/10.1017/s0022112096000420.

[56] E.A. Deem, Y. Zhang, L.N. Cattafesta, T.W. Fahringer, B.S. Thurow, On the resolution of plenoptic PIV, Meas. Sci. Technol. 27 (2016) 84003.

[57] X. Zhu, B. Zhang, J. Li, C. Xu, Volumetric resolution of light field imaging and its effect on the reconstruction of light field PIV, Opt. Commun. (2020) 125263.

[58] E.J. Gutmark, F.F. Grinstein, Flow control with noncircular jets, Annu. Rev. Fluid Mech. 31 (1999) 239–272.

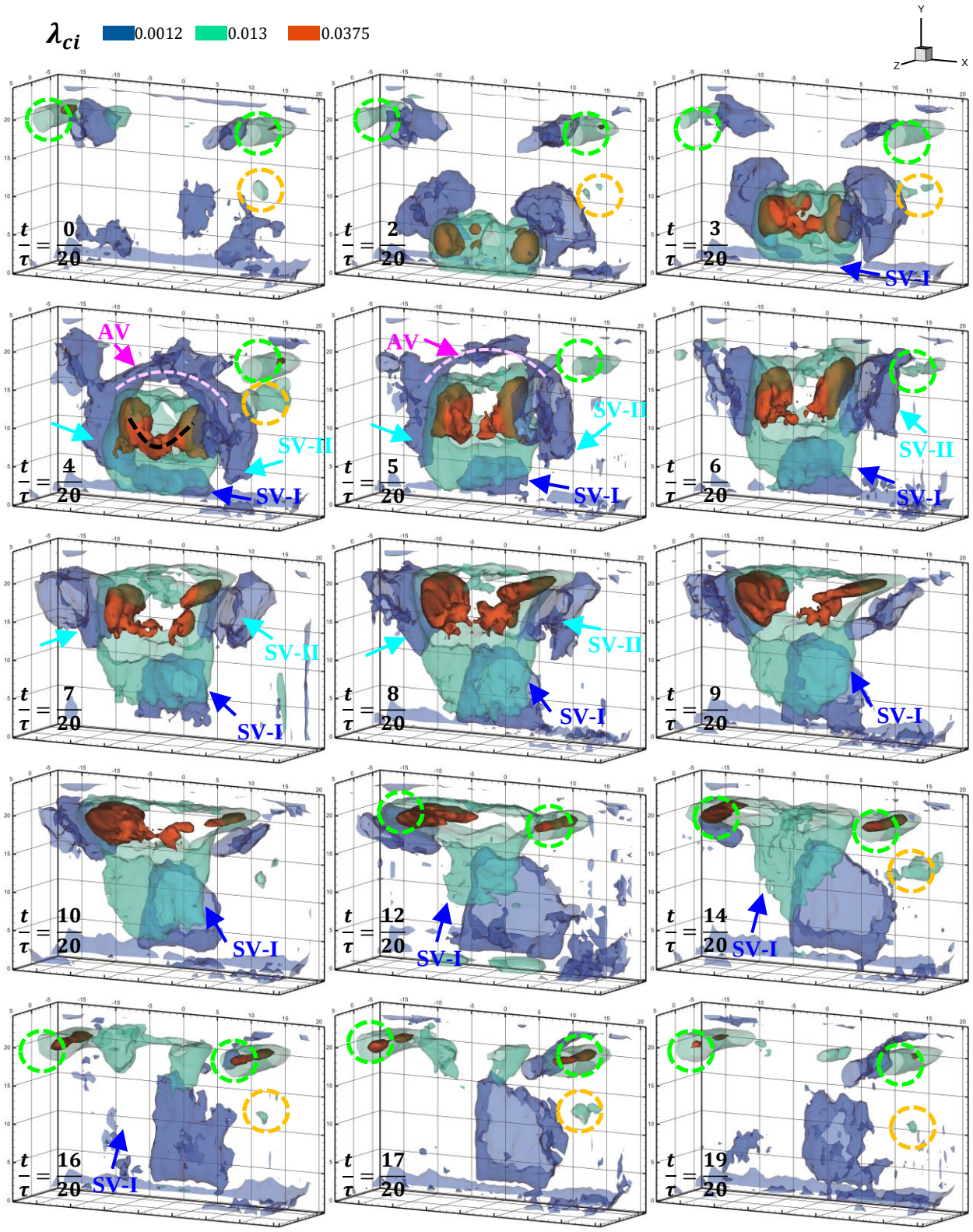
λ_{ci}
0.0012
0.013
0.0375
Y
Z
X
$\frac{t}{\tau}=\frac{0}{20}$
$\frac{t}{\tau}=\frac{2}{20}$
$\frac{t}{\tau}=\frac{3}{20}$
SV-I
AV
SV-II
$\frac{t}{\tau}=\frac{4}{20}$
$\frac{t}{\tau}=\frac{5}{20}$
$\frac{t}{\tau}=\frac{6}{20}$
$\frac{t}{\tau}=\frac{7}{20}$
$\frac{t}{\tau}=\frac{8}{20}$
$\frac{t}{\tau}=\frac{9}{20}$
$\frac{t}{\tau}=\frac{10}{20}$
$\frac{t}{\tau}=\frac{12}{20}$
$\frac{t}{\tau}=\frac{14}{20}$
$\frac{t}{\tau}=\frac{16}{20}$
$\frac{t}{\tau}=\frac{17}{20}$
$\frac{t}{\tau}=\frac{19}{20}$

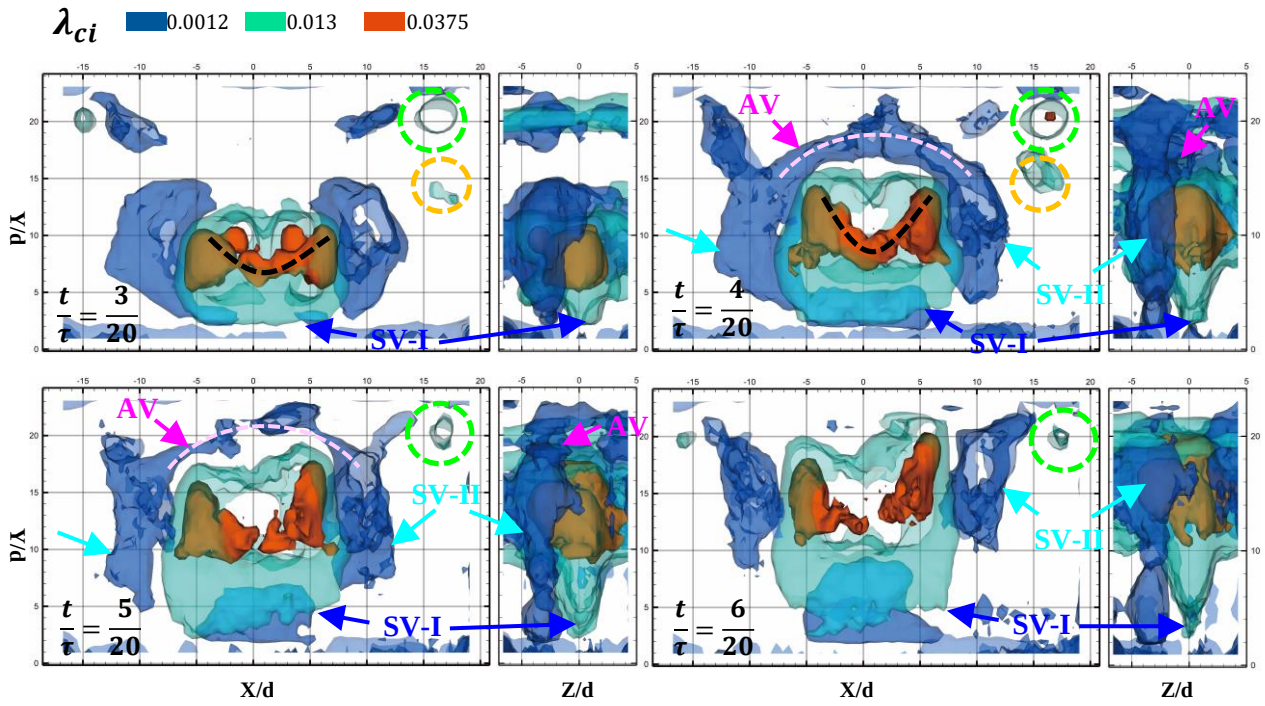
λ_{ci}
0.0012
0.013
0.0375
AV
SV-I
SV-II
$\frac{t}{\tau} = \frac{3}{20}$
$\frac{t}{\tau} = \frac{4}{20}$
$\frac{t}{\tau} = \frac{5}{20}$
$\frac{t}{\tau} = \frac{6}{20}$
Y/d
X/d
Z/d

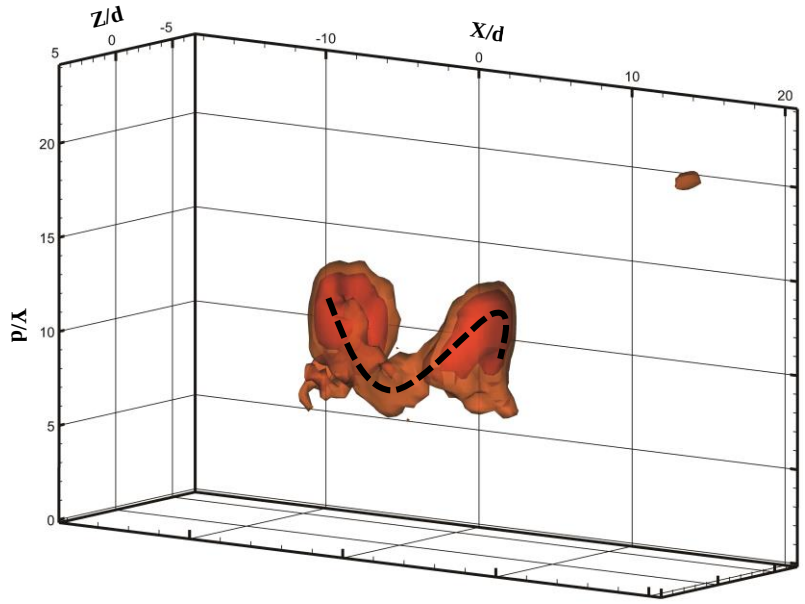
Z/d
0
-5
-10
X/d
0
10
20
5
20
15
Y/d
10
5
0

(a)

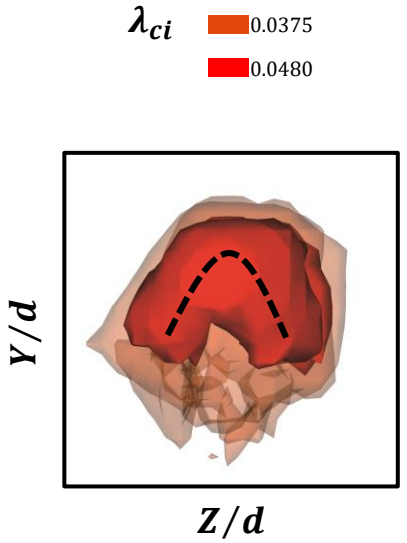
λ_{ci}
0.0375
0.0480
Y/d
Z/d

(b)

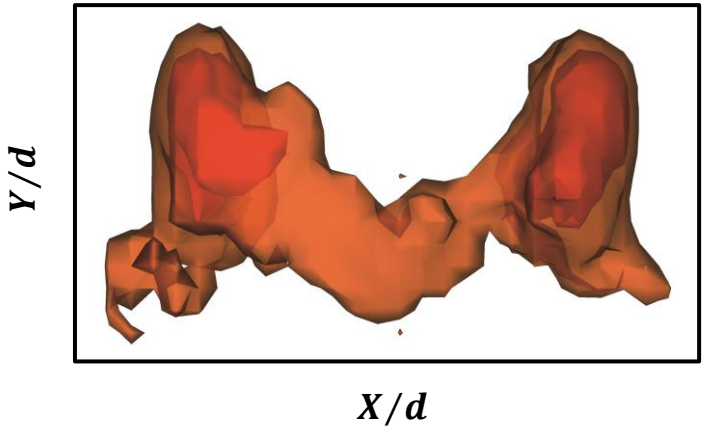
Y/d
X/d

(c)